Nuclear envelope expansion in budding yeast is independent of cell growth and does not determine nuclear volume

Alison D. Walters[a,†], Kwabena Amoateng[a,†], Renjie Wang[b], Jian-Hua Chen[c,d], Gerry McDermott[c,d], Carolyn A. Larabell[c,d], Olivier Gadal[b], and Orna Cohen-Fix[a,*]

[a]Laboratory of Molecular and Cellular Biology, National Institute of Diabetes and Digestive and Kidney Diseases, National Institutes of Health, Bethesda, MD 20892; [b]Laboratoire de Biologie Moléculaire Eucaryote, Centre de Biologie Intégrative, Université de Toulouse, CNRS, UPS, 31000 Toulouse, France; [c]Department of Anatomy, University of California, San Francisco, San Francisco, CA 94158; [d]Molecular Biophysics and Integrated Bioimaging, Lawrence Berkeley National Laboratory, Berkeley, CA 94720

ABSTRACT **Most cells exhibit a constant ratio between nuclear and cell volume. The mechanism dictating this constant ratio and the nuclear component(s) that scale with cell size are not known. To address this, we examined the consequences to the size and shape of the budding yeast nucleus when cell expansion is inhibited by down-regulating components of the secretory pathway. We find that under conditions where cell size increase is restrained, the nucleus becomes bilobed, with the bulk of the DNA in one lobe and the nucleolus in the other. The formation of bilobed nuclei is dependent on fatty acid and phospholipid synthesis, suggesting that it is associated with nuclear membrane expansion. Bilobed nuclei appeared predominantly after spindle pole body separation, suggesting that nuclear envelope expansion follows cell-cycle cues rather than cell size. Importantly, cells with bilobed nuclei had the same nuclear:cell volume ratio as cells with round nuclei. Therefore, the bilobed nucleus could be a consequence of continued NE expansion as cells traverse the cell cycle without an accompanying increase in nuclear volume due to the inhibition of cell growth. Our data suggest that nuclear volume is not determined by nuclear envelope availability but by one or more nucleoplasmic factors.**

Monitoring Editor
Anne Spang
University of Basel

Received: Apr 3, 2018
Revised: Sep 25, 2018
Accepted: Oct 24, 2018

INTRODUCTION

Many organelles and cellular structures scale with cell size (Chan and Marshall, 2010), but the mechanisms that control this scaling are poorly understood. Here we address the question of scaling between nuclear volume and cell volume, a phenomenon that is conserved in all systems examined (Jorgensen *et al.*, 2007; Neumann and Nurse, 2007; Uchida *et al.*, 2011; Walters *et al.*, 2012; Ladouceur *et al.*, 2015; Mukherjee *et al.*, 2016). The ratio between nuclear and cell volume is important for early development (Jevtic and Levy, 2015), altered in certain disease states (Chow *et al.*, 2012; Bell and Lammerding, 2016), and may be important for other, still unknown, cellular processes. For example, nuclear volume could affect the concentration of transcription activators or repressors such that an irregularly sized nucleus, as observed in certain types of cancer cells, might lead to abnormal gene expression. Because the mechanisms coupling nuclear volume to cell volume are not understood, our ability to manipulate this coupling and determine the consequences of an altered nuclear:cell (N:C) volume ratio is limited. The size of the nucleus is proportional to the amount of cytoplasm that surrounds it (Neumann and Nurse, 2007; Levy and Heald, 2010; Hara and Merten, 2015), but how the cytoplasm affects nuclear size is unclear: is nuclear size linked to a cytoplasmic structure, such as the endoplasmic reticulum (ER), or is it linked to an activity, such as

This article was published online ahead of print in MBoC in Press (http://www.molbiolcell.org/cgi/doi/10.1091/mbc.E18-04-0204) on October 31, 2018.

The authors declare that they have no competing interests.

Author contributions: A.D.W., K.A., R.W., J.-H.C., G.M., and O.C.-F. conducted the experiments. A.D.W., K.A., R.W., J.-H.C., G.M., C.A.L., O.G., and O.C.-F. designed the experiments, A.D.W. and O.C.-F. wrote the manuscript, which was edited and approved by all authors.

[†]Co–first authors.

*Address correspondence to: Orna Cohen-Fix (ornac@niddk.nih.gov).

Abbreviations used: ER, endoplasmic reticulum; GFP, green fluorescent protein; NE, nuclear envelope; NPC, nuclear pore complex; N:C, nuclear:cell; SPB, spindle pole body.

protein synthesis? Nuclear size is also affected by nuclear transport (Neumann and Nurse, 2007; Levy and Heald, 2010; Mukherjee *et al.*, 2016; Vukovic *et al.*, 2016; Kume *et al.*, 2017) and disrupting the import or levels of lamin proteins affects nuclear size (Levy and Heald, 2010; Hara and Merten, 2015; Jevtic and Levy, 2015; Jevtic *et al.*, 2015). However, whether the cell couples nuclear size and cell size through the rate of nuclear import or the amount lamins has not been established. Moreover, since both fission yeast and budding yeast maintain a constant N:C volume ratio and yet neither has lamin proteins, the N:C volume ratio, at least in these organisms, must depend on something other than lamins.

Because DNA content has been excluded as a determining factor in nuclear size (Jorgensen *et al.*, 2007; Neumann and Nurse, 2007), nuclear volume could be determined through the availability of the nuclear envelope (NE) (or components thereof) or through the synthesis and/or import of one or more nucleoplasmic components. The nucleus in both budding yeast and fission yeast is distinct from that of metazoans in at least two aspects: it lacks a lamin-based nuclear lamina, and the NE does not break down during mitosis (Walters *et al.*, 2012; Cavanaugh and Jaspersen, 2017). Instead, the NE expands as cells approach mitosis to accommodate chromosome segregation within an intact nucleus. The importance of NE expansion during yeast mitosis is underscored by the situation in the yeast *Schizosaccharomyces japonicus*, where the NE does not expand but rather ruptures during mitosis to allow for chromosome segregation (Yam et al, 2011). One of the key enzymes implicated in NE expansion is the conserved phosphatidic acid hydrolase, lipin (Pah1 in budding yeast), which converts phosphatidic acid, a precursor of major membrane phospholipids, to diacylglycerol, the precursor of the storage lipid triacylglycerol (Han *et al.*, 2006; OHara *et al.*, 2006). Pah1 is inhibited, at least in part, by phosphorylation, and it is the target of multiple kinases, including Cdc28-B type cyclins, Pho85-Pho80, Protein Kinase A, Protein kinase C, Casein kinase II, and TORC1 (Dubots *et al.*, 2014; Carman and Han, 2018). The phosphatase that activates lipin is composed of two subunits, called Spo7 and Nem1, in budding yeast. In a variety of organisms, the absence of lipin or one of the phosphatase subunits leads to ER and NE expansion, accompanied by an abnormal nuclear morphology (Tange *et al.*, 2002; Santos-Rosa *et al.*, 2005; Golden *et al.*, 2009; Gorjánácz and Mattaj, 2009). Nuclei of budding yeast *spo7*Δ, *nem1*Δ, or *pah1*Δ mutants exhibit an extension, or flare, throughout the cell cycle at the NE that is adjacent to the nucleolus (Campbell *et al.*, 2006). Conversely, overexpression of Nem1 and Spo7 prevents NE expansion (Santos-Rosa *et al.*, 2005). In wild-type cells, the expansion rate of the NE is not constant but rather accelerates as cells approach mitosis (Wang *et al.*, 2016; Blank *et al.*, 2017). The exact relationship between cell-cycle progression, the kinetics of NE expansion and the enzymes that regulate NE expansion still needs to be worked out. Importantly, however, since nuclear and cell volumes scale across all cell-cycle stages and in a broad range of cell sizes (Jorgensen *et al.*, 2007; Neumann and Nurse, 2007), this raises the question of whether NE expansion also scales with cell size.

To date, most studies on the N:C volume ratio have manipulated nuclear components (Levy and Heald, 2010; Hara and Merten, 2015; Jevtic *et al.*, 2015; Jevtic and Levy, 2015). Here we restricted cell size increase in budding yeast to determine whether the NE determines nuclear size. In doing so, we were able to examine whether, and how, the nucleus adapted to cell size and whether the NE plays a role in determining nuclear volume. Our data show that the NE expands independently of cell size, that the volume of the nucleus is not determined by the amount of NE, and that nuclear deformation allows nuclear envelope expansion without modification of nuclear volume.

RESULTS

Using *sec* mutants as a model for studying the role of NE expansion in nuclear size control

The scaling of nuclear volume and cell volume indicates that something in the cell controls nuclear size. The size of the nucleus could be determined by the availability of one of two elements: the nuclear surface area, namely the NE, or nuclear content, namely one or more constituents of the nucleoplasm. For example, the NE could expand proportionately to cell size, such that the amount of available NE would determine how large the nucleus can be. Alternatively, one or more nucleoplasmic proteins could be synthesized or imported into the nucleus in a manner that scales with cell size. In this case, the volume of the nucleus would be dependent on its content rather than its surface area, and the NE may or may not expand proportionately with cell size: increased nuclear content could drive NE expansion, or the NE could expand independently, according to cell-cycle cues (Winey *et al.*, 1997; Santos-Rosa *et al.*, 2005; Wang *et al.*, 2016; Blank *et al.*, 2017). To examine the involvement of the NE in determining nuclear volume we restricted the ability of the cell to expand (henceforth cell growth): if NE expansion is linked to cell size, then under conditions that restrict cell growth NE expansion will be inhibited as well (Figure 1, scenario 1). Alternatively, if NE expansion is independent of cell growth and instead follow cell-cycle cues, then continued NE expansion when cell growth is inhibited would result in either an abnormally large nucleus (and large N:C volume ratio), suggesting that nuclear volume could be determined by NE availability (Figure 1, scenario 2), or a deformed nucleus with an expanded NE but a normal N:C volume ratio, suggesting that something other than NE availability determines nuclear volume (Figure 1, scenario 3).

To inhibit cell growth we inactivated components of the secretory (sec) pathway (Novick and Schekman, 1979; Novick *et al.*, 1980), which is required for the trafficking of lipids and proteins between intracellular compartments and between these compartments and the plasma membrane (Feyder *et al.*, 2015). At the nonpermissive temperature, temperature-sensitive *sec* mutants restrict cell expansion but maintain phospholipid synthesis (Novick and Schekman, 1979; Ramirez *et al.*, 1983) so that, in principle, NE expansion could still occur. Moreover, although *sec* mutant cells do not bud, they do progress through the cell cycle, at least to some extent (Anastasia *et al.*, 2012, and see below), allowing us to determine whether NE expansion scales with cell growth or follows cell-cycle cues. It was also important to ensure that the conditions that arrest cell growth do not lead to abnormal expansion of the ER,

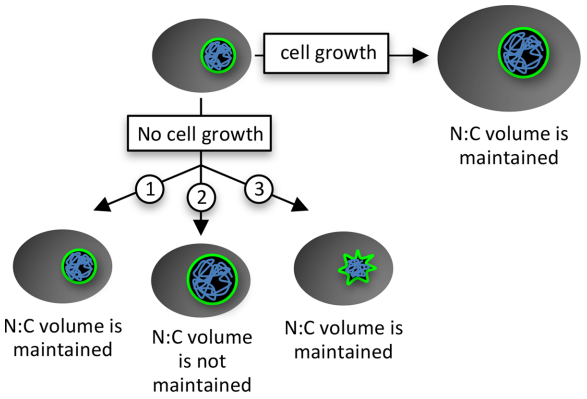

FIGURE 1: Possible outcomes of nuclear size and shape when cell growth is inhibited. See the text for more details.

which, in turn, could lead to unscheduled NE expansion. Indeed, certain *sec* mutants have been shown to affect ER structure (Novick *et al.*, 1980; Duden *et al.*, 1994; Kimata *et al.*, 1999; Higashio *et al.*, 2000; Prinz *et al.*, 2000; Ryan and Wente, 2002). However, strains carrying mutations in *SEC2*, *SEC3*, *SEC4*, *SEC6*, *SEC9*, or *SEC15* were reported to have normal ER by visual inspection (Novick *et al.*, 1980; Prinz *et al.*, 2000). Thus, we confined our analysis to mutants in these *sec* genes.

We first determined whether strains carrying mutation in the aforementioned *SEC* genes behaved as previously reported. The selected *SEC* genes code for proteins that function as part of the exocyst complex (Sec3, Sec6, and Sec15) (Heider and Munson, 2012) in post-Golgi transport (Sec4) (Feyder *et al.*, 2015) and as a t-SNARE component (Sec9) (Bombardier and Munson, 2015). All *sec* alleles exhibited temperature sensitive growth at both 34° and 37°C (Supplemental Figure S1A). At 34°C, cell growth was severely inhibited although not completely blocked (Supplemental Figure S1B and unpublished data). Finally, to examine ER expansion in these strains, the ER of all *sec* mutants used in this study was analyzed using the method described by Shibata *et al.* (2010). Briefly, ER expansion is manifested in the accumulation of ER sheets in the peripheral ER. To determine the fraction of ER sheets, the entire ER was labeled with an ER lumenal marker (DsRED-HDEL) and ER tubes were labeled with the reticulon Rtn1 fused to green fluorescent protein (GFP), which localizes only to curved membranes. Qualitatively, the ER of the *sec* mutants was similar to that of wild-type cells, as reported previously (see Novick *et al.*, 1980, Prinz *et al.*, 2000, and Supplemental Figure S2). To quantify ER expansion, the peripheral ER that contains DsRED-HDEL but not Rtn1-GFP was defined as ER sheets, which was then quantified as described in Shibata *et al.* (2010) (see also *Materials and Methods*). As a control we used a strain deleted for the *SPO7* gene, which was shown to exhibit ER expansion (Campbell *et al.*, 2006). The percentage of ER sheets in *sec3*, *sec4*, *sec6*, *sec9*, and *sec15* strains was indistinguishable from that of wild-type cells, while in *spo7*Δ strains ER sheets were significantly expanded (Figure 2 and Supplemental Figure S2). On the basis of these results we concluded that the selected *sec* mutant strains are suitable for our study.

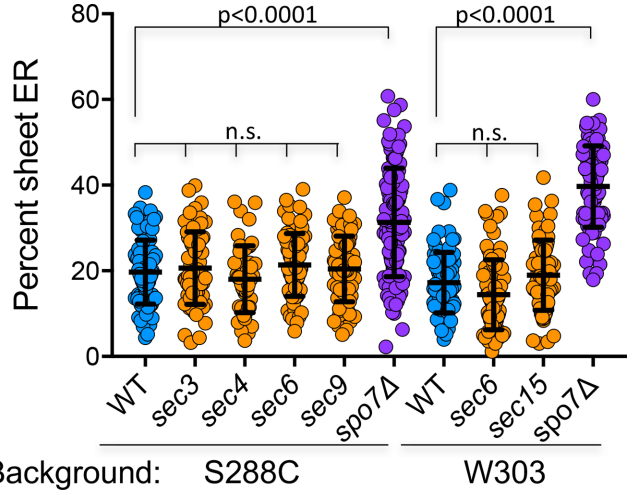

FIGURE 2: The *sec* mutants used in this study display a normal ER. Shown are the percentages of ER in the form of sheets in wild type, various *sec* mutants, and *spo7*Δ cells. Images of live cells were acquired 2 h after the shift to 34°C. $n = 86$ (WT, S288c), 70 (*sec3,* S288c), 50 (*sec4,* S288c), 78 (*sec6,* S288c), 71 (*sec9,* S288c), 110 (*spo7*Δ, S288c), 80 (WT, W303), 80 (*sec6,* W303), 80 (*sec15,* W303), and 80 (*spo7*Δ, W303) from two to three biological replicates. Error bars represent SD. Statistical analyses were done using ordinary one-way ANOVA (analysis of variance). Representative images are shown in Supplemental Figure S2.

Mutations in the secretory pathway lead to bilobed nuclei

To determine nuclear morphology, cells expressed either a nucleoplasmic protein, Pus1, fused to GFP (Figure 3A), or a nuclear pore complex subunit, Nup49, fused to GFP, which highlights the NE (Figure 3B). In addition, all strains expressed a nucleolar protein, Nsr1 or Nop1, fused to mCherry (Figure 3, A and B, respectively). In wild-type cells, nuclei were mostly round, with the nucleolus forming its typical crescent shaped structure at the edge of the nucleus, adjacent to the bulk of the DNA. In contrast, incubating *sec* mutant cells at nonpermissive temperatures of 34°C or 37°C for 2 h led to a striking bilobed nuclear phenotype, with the nucleolus occupying one lobe and the bulk of the DNA occupying the other (Figure 3, A–C). Bilobed nuclei in *sec* mutant cells accumulated gradually, reaching in many cases >60% of cells after 2 h at 34°C (Figure 3, C and D).

Alteration in nuclear morphology in *sec* mutants have been described before (Kimata *et al.*, 1999; Higashio *et al.*, 2000; Matynia *et al.*, 2002; Ryan and Wente, 2002; Perry *et al.*, 2009) but the possible significance of this phenotype in the context of cell size, nuclear size, and the N:C volume ratio was not explored. Nanduri *et al.* (1999) reported that at 37°C certain *sec* mutants exhibit defects in the localization of nuclear and nucleolar proteins, as well as in nuclear pore complex assembly. The latter was also observed by Ryan and Wente (2002). However, not all *sec* mutants exhibit this phenotype, as shown by Ryan and Wente (2002), who speculated that this phenotype is confined to *sec* mutants that exhibit defect in ER structure. In our experiments, which were performed at a lower temperature than Nanduri *et al.* (1999) and included only *sec* mutants that exhibit a normal ER structure, nuclear, nucleolar, and nuclear pore complex proteins appear to localize properly to their respective compartments. For most of the *sec* mutants included in this study, the bilobed nuclear phenotype was more penetrant at 34°C (Figure 3C), perhaps because at 37°C some *sec* mutants die before they reach the point where the bilobe forms (see below). For this reason, all subsequent experiments were done at 34°C. Because the *sec6-4* mutant strain in the W303 background was well behaved at the permissive temperature (i.e., normal growth rate and overall round nuclei), this was the main strain used for further analysis, occasionally along with a *sec15-1* strain.

Formation of bilobed nuclei requires fatty acid and phospholipid synthesis

How does the bilobed nucleus form? In theory, the *sec* pathway could be required to maintain a normal nuclear volume, such that when Sec proteins are inactivated the volume of the nucleus decreases without a corresponding decrease in nuclear surface area, causing indentation of the NE (e.g., the nucleus "deflates"). Alternatively, the nuclear bilobe could form due to continued NE expansion without a corresponding increase in nuclear volume, similarly to scenario 3 in Figure 1. In this case, nuclear deformation would likely depend on fatty acid and/or phospholipid synthesis to support NE expansion. To test this, *sec6-4* and *sec15-1* cells were treated with cerulenin, a specific inhibitor of fatty acid synthesis that allows treated cells to progress through the cell cycle (Inokoshi *et al.*, 1994; Yam *et al.*, 2011; Vadia *et al.*, 2017; and unpublished data). When cerulenin was added at the same time as shifting *sec* mutants to 34°C, the bilobed nuclear phenotype was almost completely suppressed (Figure 4, A and B). To inhibit phospholipid synthesis,

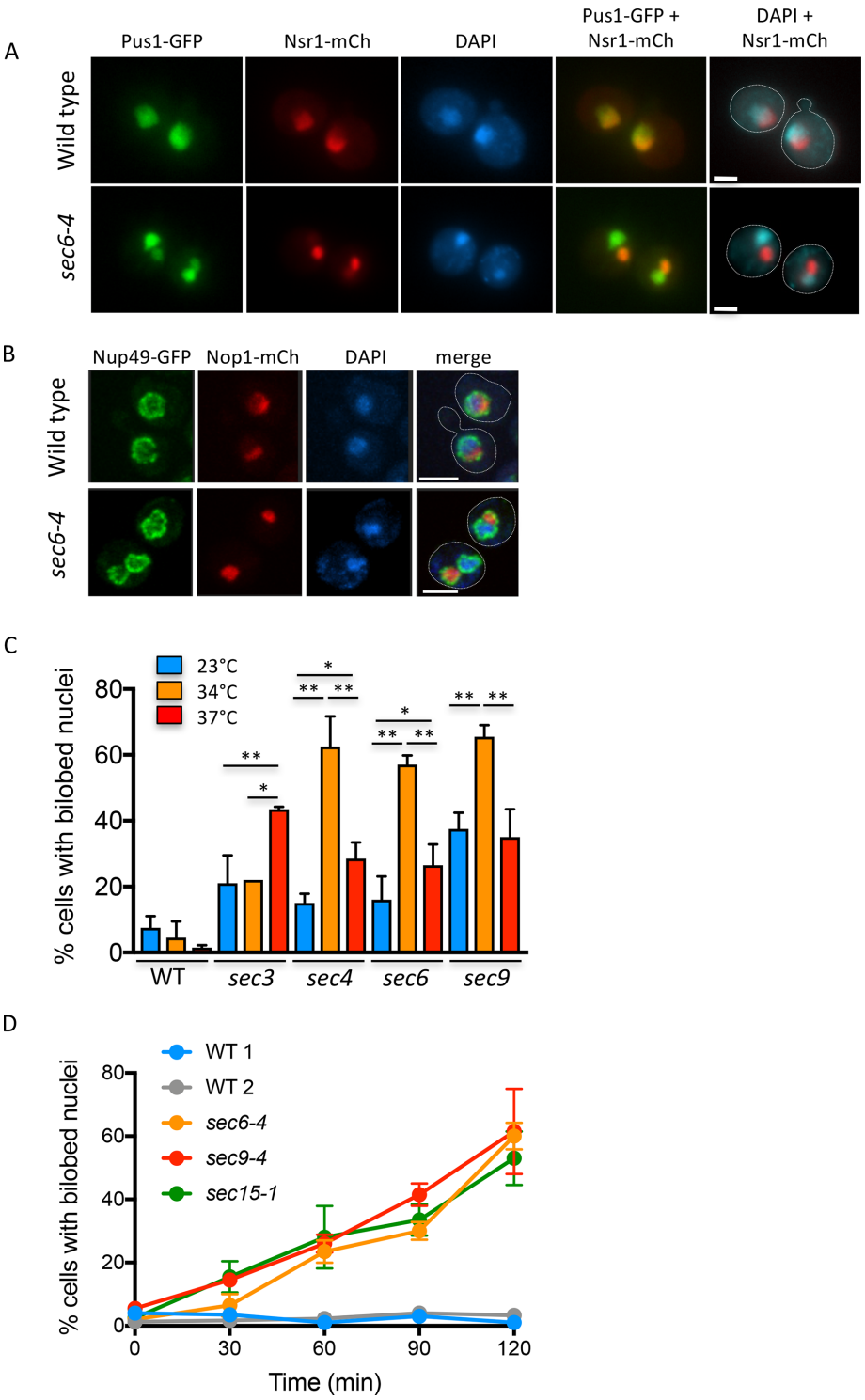

FIGURE 3: Inactivation of the secretory pathway results in the formation of bilobed nuclei. (A) Fluorescence images of wild-type and *sec6-4* cells expressing Pus1-GFP (nucleoplasm; green) and Nsr1-mCherry (nucleolus; red) that were grown at 34°C for 2 h. Cells were stained with 4′,6-diamidino-2-phenylindole (DAPI) to visualize DNA (blue). Dashed white lines outline cells. Scale bar is 2 μm. (B) Fluorescence images of wild-type and *sec6-4* cells expressing Nup49-GFP (NE; green) and Nop1-mCherry (nucleolus; red) were treated as described in A. Scale bar is 3 μm. (C) Quantification of nuclear phenotypes for WT and the indicated *sec* mutant cells shifted to 23°, 34°, or 37°C for 2 h. Nuclear phenotypes were scored using Pus1-GFP and DAPI. For each condition $n = 200$ from two biological replicates. *$p < 0.05$, **$p < 0.001$. Statistical analyses were done using Fisher's exact test. Error bars represent SD. (D) Kinetics of bilobed nuclei accumulation in wild-type, *sec6-4*, *sec9-4*, and *sec15-4* cells expressing Pus1-GFP that were incubated at 34°C for the indicated times. Wild type 1 is isogenic to *sec6-4* and *sec15-1* and wild type 2 is isogenic to *sec9-4*. For each time point, 200 cells were scored in two biological replicates. Error bars represent SD (the error bars for the WT strains are too small to be seen on the graph).

the phosphatidic acid hydrolase Pah1/lipin was hyperactivated by overexpressing the subunits of its phosphatase, Spo7 and Nem1, a condition that was previously shown to inhibit NE expansion (Siniossoglou *et al.*, 1998; Santos-Rosa *et al.*, 2005). When Pah1 is hyperactivated, the levels of phosphatidic acid in the cell drops. This has a twofold effect: it reduces the levels of the precursor for the synthesis of a number of phospholipids, and it releases the transcriptional repressor Opi1 that inhibit the expression of *CHO1*, which codes for a key enzyme in the synthesis of major membrane phospholipids, phosphatidylcholine and phosphatidylethanolamine (Han and Carman, 2017). As in the case of cerulenin treatment, overexpression of *SPO7* and *NEM1* suppressed bilobed nuclei formation in *sec6-4* cells (Figure 4C). Taken together, these results suggest that bilobed nuclei form due to continued NE expansion despite the inhibition of cell growth.

Formation of bilobed nuclei is linked to cell-cycle progression

For the *sec* mutant experimental system to be suitable for studying normal regulation of nuclear size, nuclear envelope expansion must occur as part of cell-cycle progression rather than be induced by inactivation of *SEC* genes. As noted above, the *sec* mutants employed here exhibited a normal ER structure, and thus formation of bilobed nuclei in these strains was not a consequence of irregular ER expansion. A normal ER shape further suggests that these *sec* mutants do not experience unscheduled phospholipid synthesis, as this would result in the formation of ER sheets such as those seen in *spo7*Δ and *opi1*Δ mutants (Tange *et al.*, 2002; Campbell *et al.*, 2006; Schuck *et al.*, 2009). Finally, NE expansion due to unscheduled phospholipid synthesis should result in a nuclear deformation that is cell-cycle independent, as is the case in *spo7*Δ mutants (Campbell *et al.*, 2006), while NE expansion that occurs due to the normal cell-cycle schedule should result in a nuclear deformation as cell approach mitosis, such as in the case of the mitotic flare (Witkin *et al.*, 2012). Thus, we determined whether the appearance of bilobed nuclei in *sec6-4* mutant cells is confined to a particular cell-cycle phase. Because *sec* mutants do not

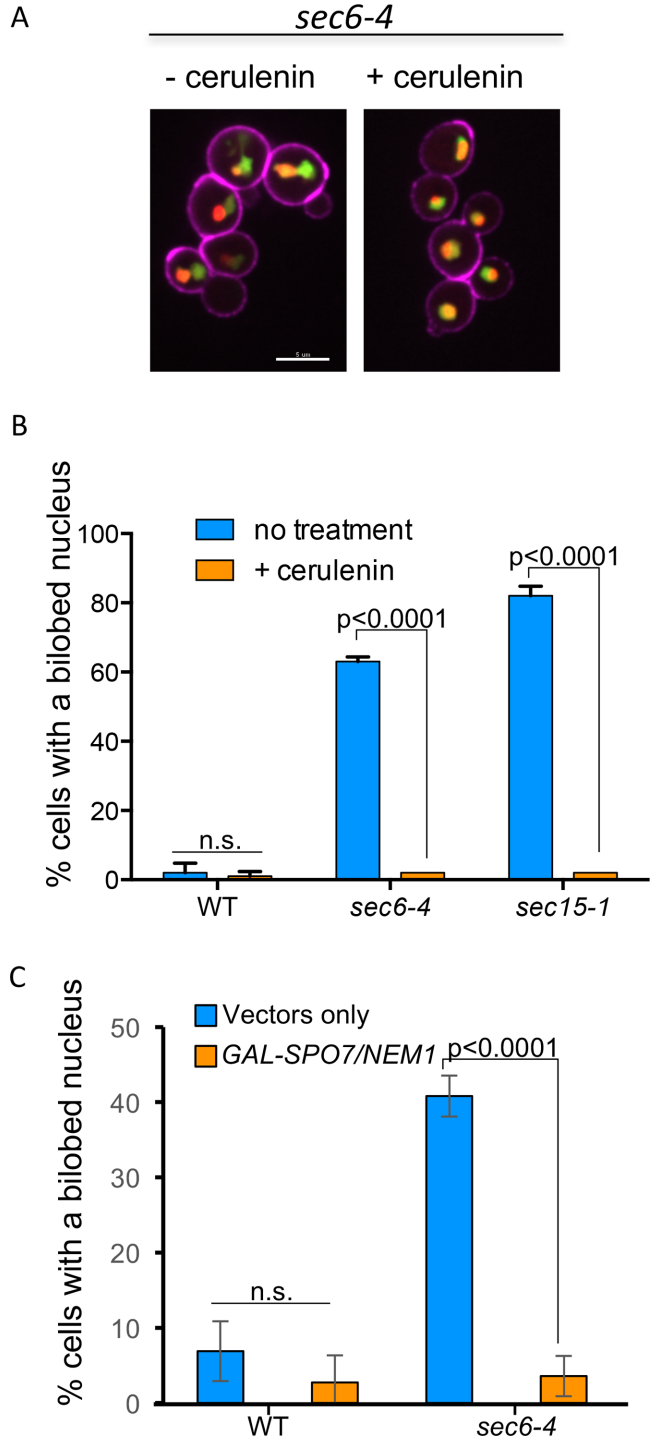

FIGURE 4: Nuclear bilobes are dependent on fatty acid and phospholipid synthesis. (A) Merged fluorescence images of untreated *sec6-4* cells (left) and cerulenin-treated *sec6-4* cells (right) grown for 2 h at 34°C. Images are a single slice from a confocal stack. The nucleoplasm is marked with Pus1-GFP (green), the nucleolus with Nsr1-CR (red), and the cell wall is stained with concanavalin A-Alexa Fluor 655 (magenta). Scale bar is 2 µm. (B) Quantification of percent cells with bilobed nuclei for WT, *sec6-4*, and *sec15-1* cells expressing Pus1-GFP grown as described in A in the presence or absence of cerulenin. $n = 200$ from two biological replicates. Error bars represent SD. Statistical analyses were done using Student's *t* test. (C) Wild-type (WT) and *sec6-4* cells expressing Nup49-GFP and carrying either empty vectors or plasmids expressing *SPO7* and *NEM1* from galactose inducible promoters were treated with galactose for 1 h at 23°C, shifted to 34°C for 2 h in the presence of galactose, and then fixed and analyzed. Four hundred cells from four biological replicates were scored for each condition. Error bars represent SD. Statistical analyses were done using Student's *t* test.

bud but they progress through the cell cycle at least until G2 (Anastasia *et al.*, 2012), we followed cell-cycle progression through spindle pole body (SPB) separation, using the SPB component Spc42 fused to mCherry. Budding yeast SPBs are embedded in the NE throughout the cell cycle, where they nucleate microtubules and, after SPB duplication, anchor the poles of the spindle (Cavanaugh and Jaspersen, 2017). Daughter cells inherit a single SPB, which then duplicates in S phase in a cell-cycle-regulated manner, followed by SPB separation. Thus, a single focus of Spc42-mCherry is indicative of cells in G1/early S, before SPB duplication, while two separated foci are indicative of cells in G2/M (Cavanaugh and Jaspersen, 2017).

An asynchronous culture of wild-type and *sec6-4* cells expressing Pus1-GFP and Spc42-mCherry were grown to early log phase at 23°C and then imaged at 15-min intervals for 2 h at 34°C. Nuclear shape and the distance between SPBs at each time point were determined for 50 *sec6-4* cells that formed a bilobed nucleus at any point during the time course. *sec6-4* cells with bilobed nuclei were divided into three classes: cells that started the experiment with a single SPB that duplicated during the course of the experiment (designated Group 1; $n = 27$, Supplemental Table S1), cells that started with two SPBs (designated Group 2; $n = 17$, Supplemental Table S1), and cells that started with a single SPB that did not duplicate throughout the course of the experiment (designated Group 3; $n = 6$, Supplemental Table S1). To determine whether SPB separation occurred in a timely manner in the *sec6-4* mutant, the time at which two SPBs were first observed was compared between Group 1 *sec6-4* cells and wild-type cells that started with a single SPB (Supplemental Table S2, $n = 25$). The starting cultures in both strains were asynchronous, but nonetheless the average time to SPB separation was similar (Figure 5A, 54.00 ± 4.74 min and 59.44 ± 4.56 min for wild-type and *sec6-4* cells, respectively, $p = 0.4121$, Student's *t* test), indicating that SPB separation is a suitable cell-cycle marker for *sec6-4* cells. When considering all three groups together, 78% of bilobed nuclei in *sec6-4* cells appeared in cells with two SPBs (Supplemental Table S1). When considering only Group 1, which started with a single SPB that then duplicated and separated, 81.5% of bilobed nuclei occurred after SPB separation (Figure 5B, Supplemental Figure S3A, and Supplemental Table S1), suggesting that bilobed nuclei appear preferentially later in the cell cycle.

There could be two reasons for the appearance of biolobed nuclei after SPB separation: the bilobed nuclei could have appeared after a certain amount of time at 34°C, or the formation of bilobed nuclei could have been dependent on cell-cycle–dependent NE expansion that occurs as cells enter mitosis. If the former were true, then bilobed nuclei should appear at a fixed time following the temperature shift, regardless of where in the cell cycle the cells were at the time of the temperature shift. However, cells that had two SPBs at the time of the temperature shift developed bilobed nuclei significantly faster than cells that had only one SPB at the time of the temperature shift (Figure 5C and Supplemental Figure S3B), consistent with the nucleus becoming bilobed as a function of cell-cycle progression. Taken together, our data suggest that bilobed nuclei are a consequence of cell-cycle–regulated NE expansion. This could also explain the higher penetrance of the bilobed phenotype at 34°C compared with 37°C (Figure 3C) if, at the higher temperature,

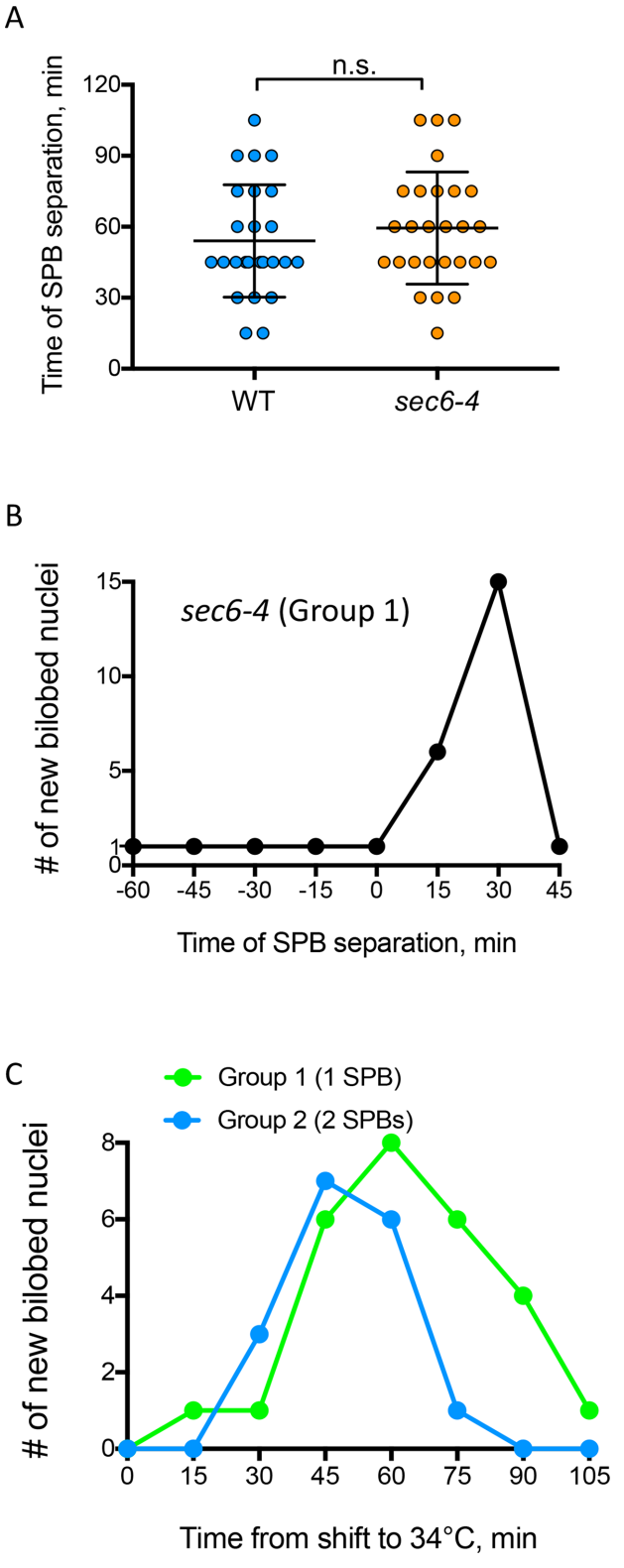

FIGURE 5: The bilobe nuclear phenotype in *sec* mutants is more prevalent later in the cell cycle. Wild-type (WT) and *sec6-4* cells, both expressing Pus1-GFP and Spc42-mCherry, were grown at 23°C, placed on agar pads, and immediately incubated at 34°C and imaged live using a DeltaVision microscope. (A) The time point at which SPB separation was seen in WT (blue) and *sec6-4* (orange) cells that had a single SPB at time 0. $n = 25$ and 27 for WT and *sec6-4*, respectively. Error bars represent SD. Statistical analyses were done using Student's *t* test. (B) Time, relative to SPB separation, when bilobed nuclei were first observed in 27 *sec6-4* cells that were followed by live microscopy. The individual time courses are shown in Supplemental Figure S3A. (C) Time, relative to the temperature shift to 34°C, of when bilobes were first observed in *sec6-4* cells that initially had one SPB (Group 1, green) or two SPBs (Group 2, blue). $n = 27$ and 16 for Group 1 and Group 2, respectively.

sec mutant cells die before they reach the appropriate cell-cycle stage for nuclear bilobe formation.

As noted above, another nuclear deformation that is cell-cycle–dependent is the mitotic flare, which occurs when chromosome segregation is blocked yet the NE continues to expand. Under these conditions cells continue to grow (Johnston *et al.*, 1977) and nuclear deformation occurs because the nucleus cannot elongate as it normally would in anaphase (Witkin *et al.*, 2012). Unlike mitotically arrested cells, *sec* mutants likely accumulate in a Swe1-dependent G2 arrest (Anastasia *et al.*, 2012). Nonetheless, the bilobe and flare could be different manifestations of the same nuclear phenotype, as they both occur late in the cell cycle and both involve a deformation that reduces the contact between the nucleolus and the nuclear compartment that contains the bulk of the DNA. We have previously shown that mitotic nuclear flare formation is dependent on the Polo-like kinase, Cdc5 (Walters *et al.*, 2014). To determine whether the *sec* mutant nuclear bilobe also depends on Cdc5, *sec6-4*, and *sec6-4*, *cdc5-nf* cells expressing Pus1-GFP were grown to early log phase at 23°C and arrested in G1 with alpha factor mating pheromone. Once the arrest was complete (>95% of cells), cells were released to 34°C for 2 h. Unlike mitotic flares, which are dependent on the Polo-like kinase Cdc5 (Walters *et al.*, 2014), nuclear bilobes in *sec6-4* cells are not (Supplemental Figure 4A). The same result was obtained when the two strains were shifted for 2 h to 34°C without a preceding G1 arrest (unpublished data). Thus, the nuclear bilobe and the mitotic flare are distinct phenomena.

Cycloheximide treatment is accompanied by alterations in ER structure

Inhibition of secretion is not the only condition known to inhibit cell growth in budding yeast. To examine the nuclear response to other known cell growth inhibitors we treated cells with cycloheximide, a protein synthesis inhibitor, and rapamycin, an inhibitor of mechanistic target of rapamycin (mTOR) (Hereford and Hartwell, 1974; Gonzalez *et al.*, 2009). Cycloheximide induced a rapid, fatty acid synthesis–dependent deformation of the nucleus (Figure 6, A and B, and Supplemental Figure S4B; compare with Figure 3D), consistent with the induction of unscheduled NE expansion. Indeed, examination of ER morphology using Rtn1-GFP and DsRED-HDEL as described above revealed that cycloheximide treatment leads to ER expansion (Figure 6C and Supplemental Figure S4C). It was previously shown that cycloheximide treatment causes a rapid, TORC1-dependent phosphorylation of a number of downstream targets of the TOR pathway (Urban *et al.*, 2007; Lempiainen *et al.*, 2009). Since the TOR pathway also regulates phospholipid synthesis (Dubots *et al.*, 2014), cycloheximide treatment may lead to an unscheduled, TOR-dependent induction of phospholipid synthesis, resulting in the expansion of both the ER and the NE.

Rapamycin treatment did not lead to any nuclear deformation, likely because rapamycin inhibits the TOR pathway, thereby repressing phospholipid synthesis (Dubots *et al.*, 2014). Indeed, treatment of *sec6-4* cells with rapamycin suppressed the bilobed nuclear phenotype (Supplemental Figure S4D). Thus, inhibition of secretion is the only condition we have identified so far that inhibits cell growth without affecting the normal schedule of NE expansion.

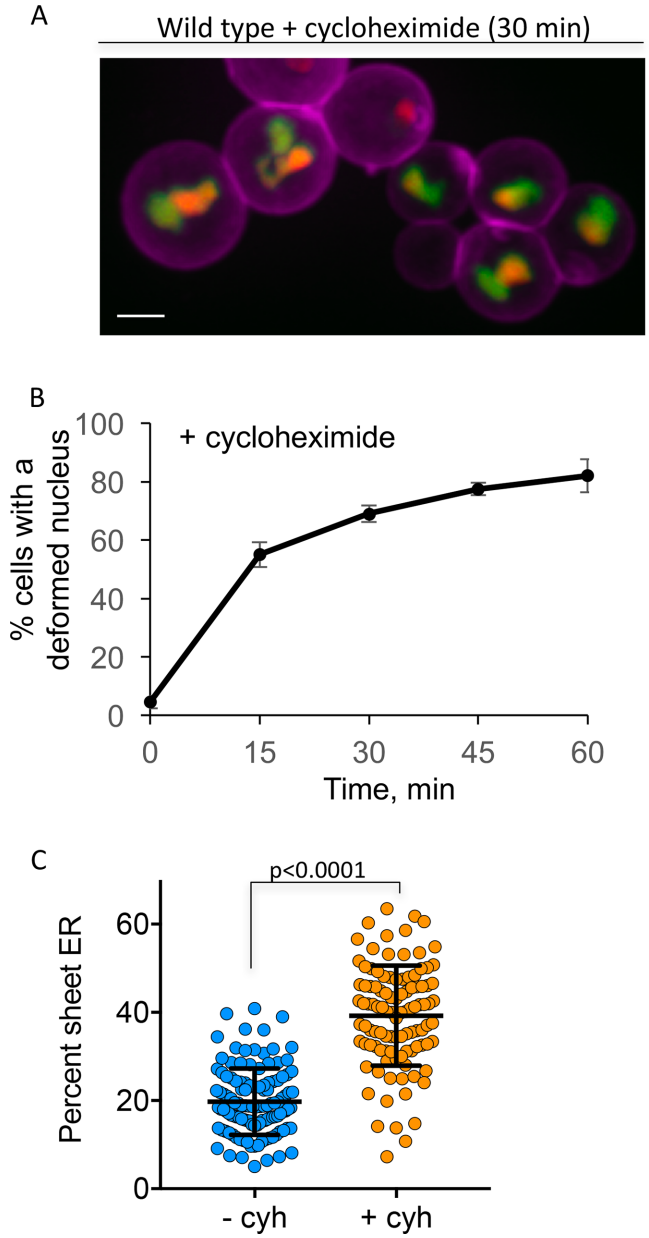

FIGURE 6: Cycloheximide treatment leads to NE deformation and unscheduled ER expansion. (A) An image of WT cells expressing Pus1-GFP and Nsr1-mCherry treated with cycloheximide for 30 min, fixed, stained with ConA-AlexaFluor 655 and imaged by confocal microscopy. Cycloheximide-induced deformed nuclei were more irregular than bilobed nuclei. (B) Kinetics of deformed nuclei formation in WT cells expressing Pus1-GFP, treated with cycloheximide at 34°C for the indicated times. Two hundred cells per time point were counted in two biological replicates. (C) The percentage ER sheets, determined as described in Figure 2, for untreated wild-type cells or cells treated with cycloheximide. $n = 120$ cells (untreated) and 104 cells (treated) from three biological replicates. Error bars represent SD. Statistical analyses were done using Student's *t* test.

The N:C volume ratio is maintained in cells with bilobed nuclei

Our data thus far indicate that in *sec* mutants the NE continues to expand despite inhibition of cell growth. The question that remains is what happens to the N:C volume ratio in cells with bilobed nuclei (Figure 1A, scenarios 2 and 3): if it increases, then the NE may determine nuclear volume. If, however, it remains unchanged, then the NE cannot determine nuclear volume, and something else must dictate the scaling of nuclear volume with cell volume. While yeast cell size is relatively easy to estimate given that yeast cell shape can be approximated to a prolate sphere (Jorgensen *et al.*, 2007; Webster *et al.*, 2010), accurately determining nuclear size, especially when the nucleus is not spherical, is more technically challenging. Readily available methodologies relying on three-dimensional reconstructions based solely on fluorescently labeled nucleoplasmic proteins have the disadvantage of not precisely delineating the nuclear perimeter, potentially under- or overestimating nuclear volume and surface area. However, if validated, this method can be used at ease to explore various properties of nuclear dimensions. Because determining the N:C volume ratio accurately was crucial for our model, we employed three independent methods to determine nuclear and cell size: The NucQuant method (Wang *et al.*, 2016), soft X-ray tomography (McDermott *et al.*, 2012; Parkinson *et al.*, 2012), and three-dimensional reconstructions using a nucleoplasmic protein (Webster *et al.*, 2010). Note that these methods differ not only in the imaging modality but also in the way the cells are treated before imaging: live imaging for the NucQuant method, immersion in liquid nitrogen-cooled propane for soft X-ray tomography, and chemical fixation for the three-dimensional reconstruction based on fluorescence. Thus, differences in the absolute values of nuclear and/or cell volumes are to be expected. Importantly, however, all three methods supported the conclusion that *sec* mutants with bilobed nuclei maintain a normal N:C volume ratio.

The NucQuant method

To compare between the three methods, cells had to be grown under the same conditions. For reasons that are unknown, *sec6-4* mutant cells grown for 2 h at 34°C were extremely vulnerable to the liquid nitrogen treatment that is integral to the soft X-ray tomography method (Le Gros *et al.*, 2005). Therefore, all three methods used cells that were incubated at 34°C for 1 h only. In the NucQuant method, fluorescence confocal images were taken of wild-type cells and *sec6-4* cells with bilobed nuclei, both expressing GFP-Nup49 to detect nuclear pore complex (NPC) clusters on the NE, and mCherry-Nop1 to mark the nucleolus (Figure 7A). Because of uncertainty in volume reconstructions for nuclei that span the bud neck, the analysis was confined to unbudded and small budded cells where the nucleus was still within the mother cell. Consequently, at 34°C, the average cell size was greater in *sec6-4* cells, which do not bud but continue to expand slowly, compared with wild-type cells, for which large budded cells were excluded (Figure 7B). NPC clusters were used as described in Wang *et al.* (2016) to compute nuclear volume from three-dimensional reconstructions of nuclei (Figure 7A) and generate cumulative probability maps of NPC position in each population of cells (Figure 7C). These maps further demonstrated that *sec6-4* nuclei are elongated along the nuclear center–nucleolar center axis. They also show that NPC density is lower at the boundary between the two lobes of *sec6-4* bilobed nuclei (Figure 7C), at the interface of the nucleolus and the rest of the nucleus, in keeping with previously published observations (Wang *et al.*, 2016). The reduction in NPC number at this location indicates that this region of the NE may have distinct properties. These properties may play a role in defining the NE adjacent to the nucleolus as the region that deforms under a variety of conditions (Siniossoglou *et al.*, 1998; Campbell *et al.*, 2006; Witkin *et al.*, 2012). Alternatively, or in addition, NPCs, which are mobile in budding yeast (Bucci and Wente, 1997), may be less likely to occupy the concave NE at the

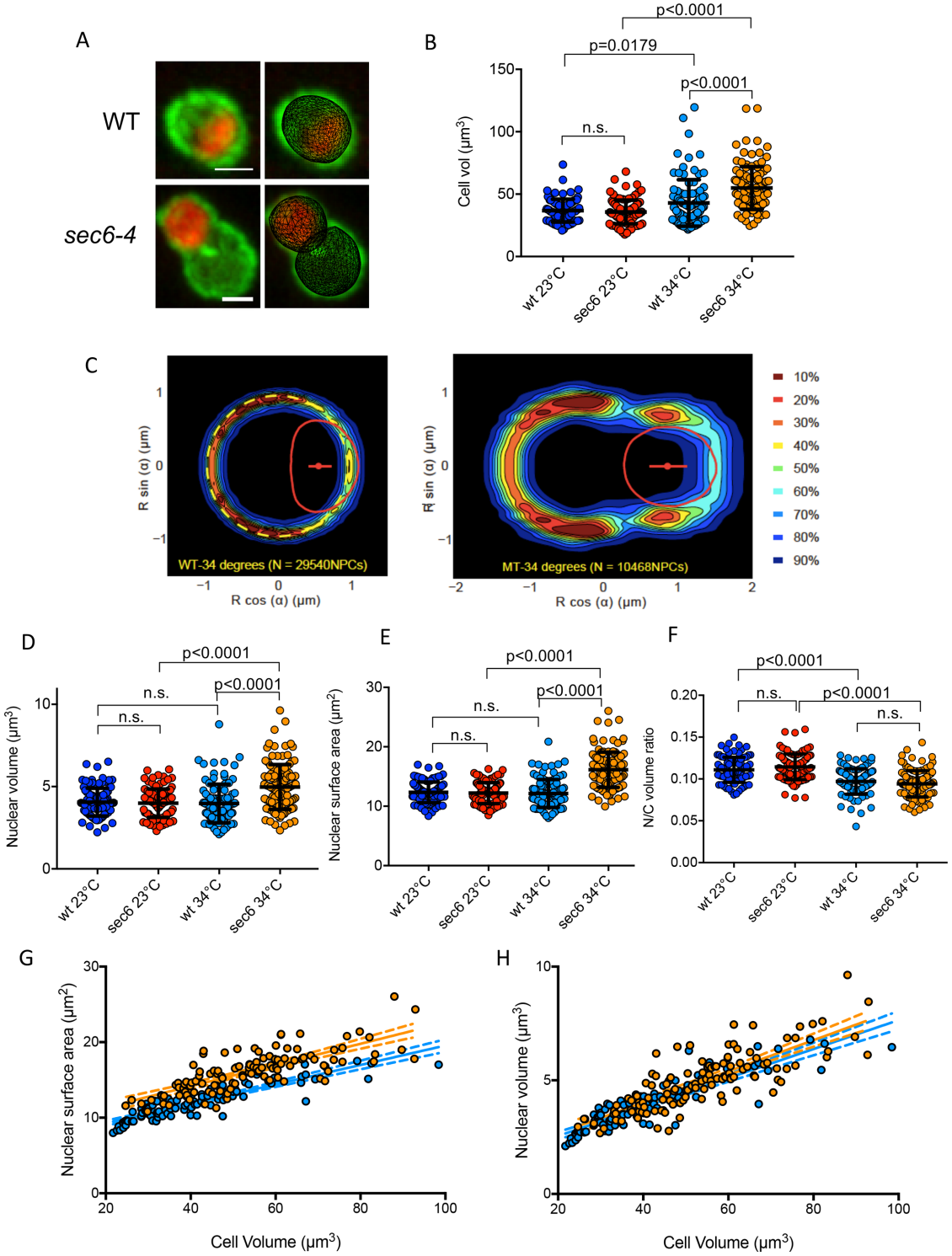

FIGURE 7: The N:C volume ratio is maintained in cells with bilobed nuclei, as determined by the NucQuant method. (A) A three-dimensional NE model fitting for nuclei from wild-type (WT) and *sec6-4* cells shifted to 34°C for 1 h. Nup49::GFP marks the NE and Nop1::mCherry marks the nucleolus. For each strain, the left panel is a maximum projection from a stack of confocal images and the right panel is the fluorescence image with the mesh representation of reconstructed 3D-NE overlaid. Scale bar is 1 μm. (B) Quantification of cell volumes for WT and *sec6-4* cells grown at 23°C or 34°C (1 h). For the *sec6-4* strain at 34°C, only bilobed cells were considered. $n = 95$ (WT at 23°C), 99 (*sec6-4* at 23°C), 96 (WT at 34°C), and 115 (*sec6-4* at 34°C). The *p* values in this panel and in D, E, and F were determined using ordinary one-way ANOVA with correction using Tukey's multiple comparison test. (C) NPC probability density maps for WT and *sec6-4*. Maps were constructed from population-aggregated densities of NPCs from 852 cells for WT and 226 cells containing bilobed nuclei for *sec6-4* as in Wang *et al.* (2016). The color scale indicates the density of NPC detection: for example, dark red indicates the smallest volume encompassing 10% of all aggregated NPCs of the population, and dark blue indicates the smallest volume encompassing 90% of all aggregated NPCs of the

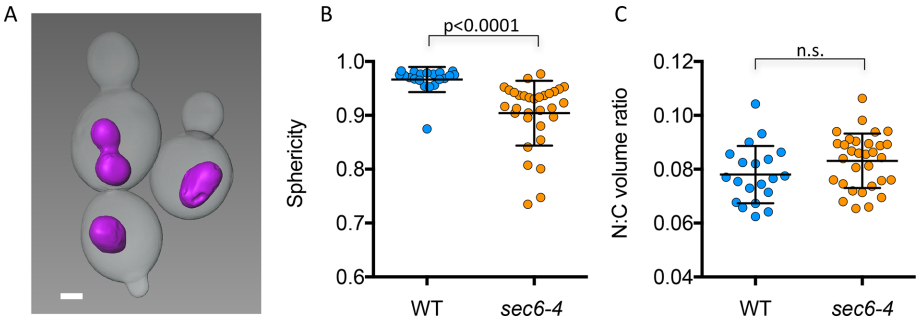

FIGURE 8: Wild-type and *sec6-4* mutant cells exhibit the same N:C volume ratios, as determined by soft X-ray tomography. (A) Surface rendered views of *sec6-4* cells shifted to 34°C for 1 h and then imaged using soft X-ray tomography. Nuclei are shown in purple. Scale bar is 1 µm. (B) Distribution of sphericity in nuclei from wild-type and *sec6-4* cells. The *p* value was calculated using Student's unpaired parametric two-tailed *t* test. $n = 20$ and 31 for wild type and *sec6-4*, respectively. (C) Distribution of N:C volume ratios for WT and *sec6-4* cells from samples as in B. There is no significant difference between the N:C volume ratios of WT and *sec6-4* cells ($p = 0.096$, Student's unpaired parametric two-tailed *t* test).

constricted region between the two nuclear lobes of the *sec6-4* mutant.

In wild-type cells, growth at 34°C led to an increase in the average cell size without an accompanying increase in the average nuclear volume or nuclear surface area (Figure 7, B, D, and E). Consequently, the N:C volume ratios of wild-type cells at 23°C were, on average, higher than at 34°C (Figure 7F). The average nuclear surface area was similar for wild-type and *sec6-4* cells at 23°C but higher for *sec6-4* cells at 34°C (Figure 7D), as expected from the bilobed nuclear phenotype of *sec6-4* cells. Likewise, nuclear volumes were similar for wild-type and *sec6-4* cells at 23°C but higher for *sec6-4* cells at 34°C (recall that the larger anaphase nuclei of wild-type cells that traverse the bud neck were excluded from the analysis). Importantly, however, the average N:C volume ratios for wild-type (WT) and *sec6-4* cells were strikingly similar at both 23° and 34°C (Figure 7F). Thus, at 34°C, wild-type cells with round nuclei and *sec6-4* cells with bilobed nuclei have the same N:C volume ratio, despite the latter having a greater nuclear surface area. In other words, while the nuclear surface area per a given cell volume was higher for *sec6-4* cells compared to wild type (Figure 7G), the nuclear volume per a given cell volume was similar for both strains (Figure 7H). Taken together, by this analysis, the NE does not determine nuclear volume. Instead, nuclear deformation allows for NE expansion without altering the N:C volume ratio.

Soft X-ray tomography

In the soft X-ray tomography approach (Parkinson *et al.*, 2012), tomographic reconstructions were generated for 20 wild-type cells with round nuclei, and 31 *sec6-4* cells with nuclei that ranged in shape from round to bilobed (Figure 8A). Nuclear shape was quantified by calculating sphericity, a measure of how mathematically close a given object is to a sphere, which is the most compact form. Sphericity is defined as the ratio of the surface area of a sphere with the same volume as the object of interest to the surface area of the object itself (Wadell, 1935). For example, a perfect sphere has a sphericity value of 1, whereas a bilobed nucleus, such as the one shown in top left of Figure 8A, can have a sphericity value as low as 0.8, since a sphere with the same volume as a bilobed object will have a smaller surface area than the bilobe. As expected, nuclei of *sec6-4* cells had reduced sphericity compared with WT (Figure 8B). Reconstructed nuclei of both wild-type and *sec6-4* cells generated from soft X-ray data were substantially smaller than the reconstructed volumes and surfaces areas in the NucQuant methodology, and, consequently, the N:C volume ratios were smaller (Supplemental Table S3). Importantly, however, and in agreement with our NucQuant reconstruction data, there was no significant difference between the N:C volume ratios of wild-type and *sec6-4* cells (Figure 8C).

Nucleoplasmic fluorescence

Finally, we analyzed the N:C volume ratios for two *sec* mutant strains, *sec6-4* and *sec15-1*, using three-dimensional reconstructions of the nucleoplasmic marker Pus1-GFP (Webster *et al.*, 2010). Overall, in this method nuclear and cell sizes were more similar to the values we obtained with the NucQuant method than soft X-ray (Supplemental Table S3), possibly because they both rely on fluorescence. Following a 1-h temperature shift, the percentage of cells with bilobed nuclei for wild type, *sec6-4*, and *sec15-1* was 3.33 ± 3.06, 30.00 ± 7.21, and 47.62 ± 10.99, respectively ($n = 150$ for each strain from three biological replicates). This allowed us to compare between cells with round versus bilobed nuclei within the same *sec* mutant strain (the wild-type strain had too few cells with bilobed nuclei to do this kind of analysis). By visual inspection, nuclei in which two lobes began to appear had a sphericity value of ~0.955 (Supplemental Figure S5, A and B). Thus, we compared sphericity, cell size, nuclear size, nuclear surface area, and N:C volume ratio for *sec6-4* and *sec15-1* cells with mostly round (sphericity ≥0.955) versus mostly bilobed (sphericity <0.955) nuclei (values for all cells in each strain are provided in Supplemental Figure S5).

By design, the round and bilobed nuclei differed significantly in sphericity (Figure 9A). As expected, bilobed nuclei had on average a greater surface area than round nuclei (Figure 9B). The *sec* mutant cells with bilobed nuclei were significantly larger than cells with

population. In other words, the highest probability of detecting NPCs is in the dark red zones while the lowest probability is in the dark blue zones. Red curve indicates the median nucleolus based on the number of cells indicated above; red line indicates the position of median nucleolar centroid; dashed yellow line indicates the median NE in WT. (D, E) Nuclear volumes (D) and nuclear surface areas (E) for cells as described in B. $n = 100$ for all conditions except *sec6-4* at 34°C, which had $n = 125$. (F) N:C volume ratios for cells as described in B. (G) Nuclear surface area as a function of cell volume for wild-type and *sec6-4* cells grown at 34°C for 1 h. $n = 94$ and 113 for wild type and *sec6-4*, respectively. Linear regression was done using Prism software. The lines for wild type and *sec6-4* can be described as $y = 0.1286*x + 6.693$ and $y = 0.1402*x + 8.567$, respectively. R^2 values are 0.7892 and 0.591 for wild type and *sec6-4*, respectively. Dashed lines represent 95% confidence. (H) Nuclear volume as a function of cell volume for wild type and *sec6-4* cells grown at 34°C for 1 h, as described in G. The linear regression lines for wild type and *sec6-4* can be described as $y = 0.06372*x + 1.277$ and $y = 0.06844*x + 1.29$, respectively. R^2 values are 0.7971 and 0.646 for wild type and *sec6-4*, respectively. Dashed lines represent 95% confidence.

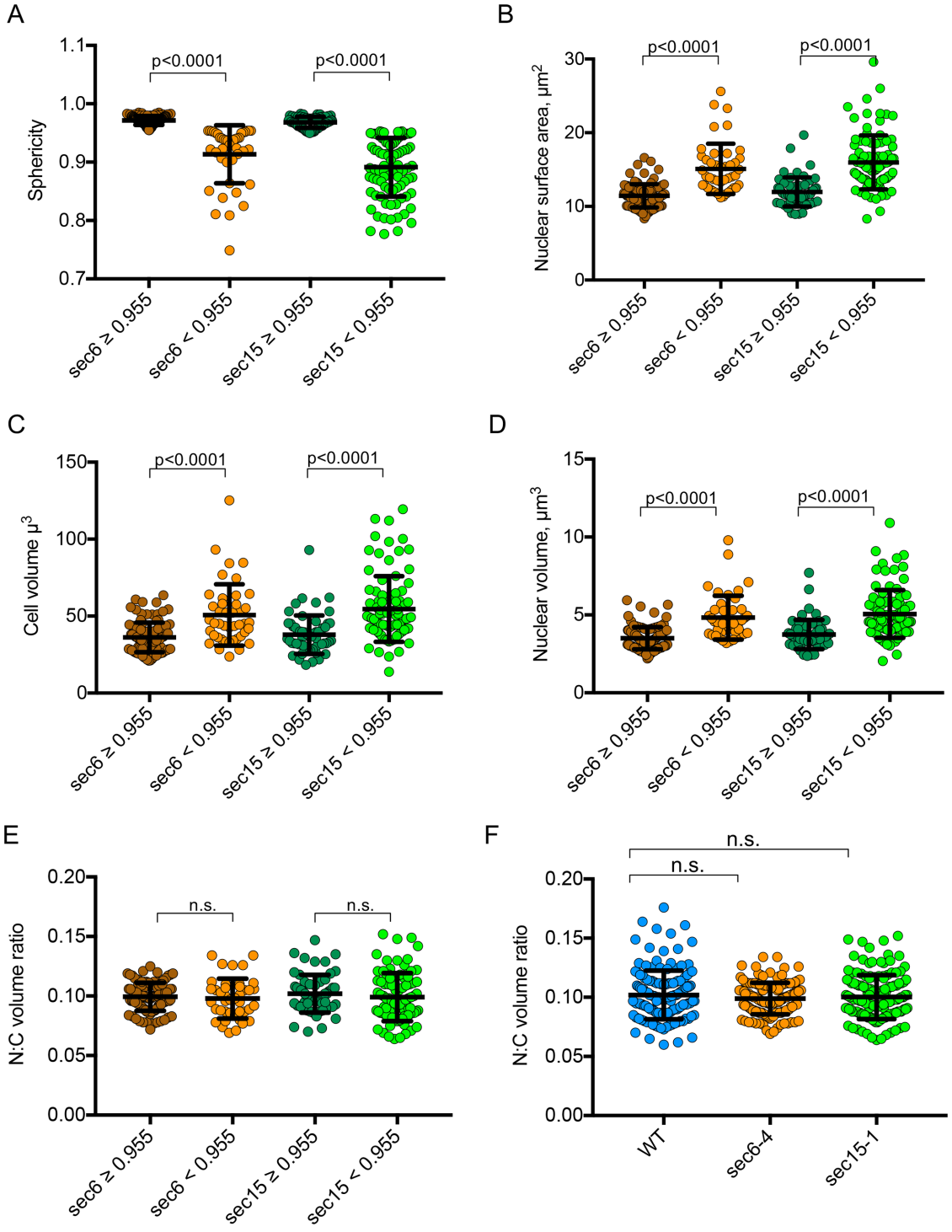

FIGURE 9: The N:C volume ratio is the same for round and bilobed nuclei within the same *sec* mutant. (A) *sec6-4* and *sec15-1* cells grown for 1 h at 34°C, fixed, and imaged were divided based on their sphericity, with a sphericity value of 0.955 being the cutoff. $n = 107$ (for *sec6* ≥ 0.0955), 42 (*sec6* < 0.955), 58 (*sec15* ≥ 0.955), and 89 (*sec15* < 0.955) from three biological replicates. Here and in all subsequent panels, *p* values were determined using one-way ANOVA with multiple comparisons. (B–E) Same cells as in A, analyzed for nuclear surface area (B), cell volume (C), nuclear volume (D), and N:C volume ratio (E). (F) The entire pool of wild-type (WT), *sec6-4*, and *sec15-1* cells were analyzed for N:C volume ratio. $n = 150$ (WT), 149 (*sec6-4*), and 147 (*sec15-1*) from three biological replicates.

round nuclei (Figure 9C), consistent with bilobed nuclei forming later in the cell cycle (recall that the inhibition of cell growth at 34°C was incomplete). Likewise, the average nuclear volume of bilobed nuclei was greater than round nuclei in both *sec* strain (Figure 9D), as expected from cells that are farther along in the cell cycle. Importantly, however, the N:C volume ratios were the same for cells with round versus bilobed nuclei (Figure 9E). Moreover, when all cells were considered, there was no difference in the N:C volume ratio

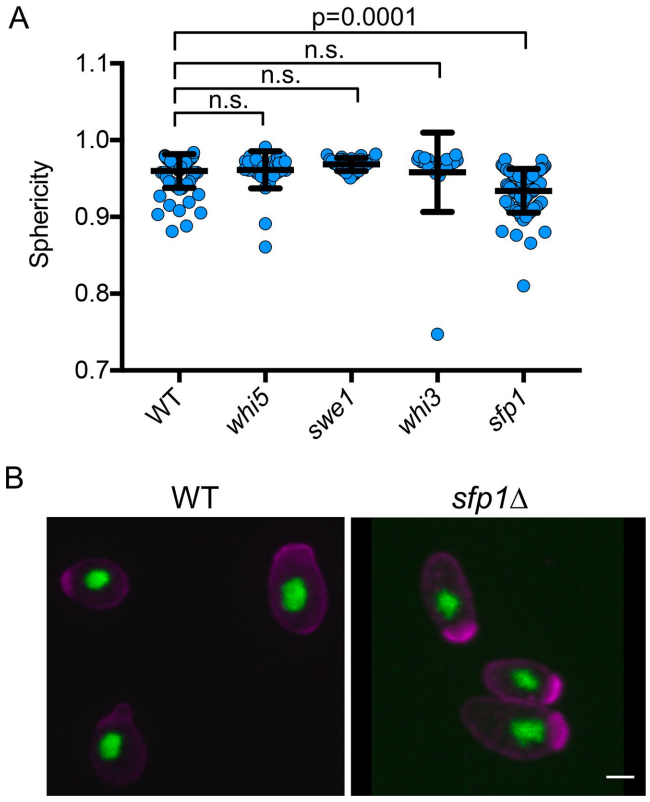

FIGURE 10: Nuclear shape in small sized cell mutants is mutant specific. (A) Sphericity of nuclei from WT ($n = 81$), *whi5*Δ ($n = 34$), *swe1*Δ ($n = 31$), *whi3*Δ ($n = 19$), and *sfp1*Δ ($n = 74$) cells expressing Pus1-GFP were grown in YPD at 30°C to replicate published conditions in which these mutants exhibited a small cell size. The *p* values were determined by one-way ANOVA with correction for multiple comparisons. (B) Fluorescence images of WT and *sfp1*Δ cells expressing Pus1-GFP (green) and strained with ConA-AlexaFluor 655 (purple). Scale bar is 3 μm.

between wild type and each of the *sec* mutants (Figure 9F). Thus, despite possessing a greater nuclear surface area, cells with bilobed nuclei have the same N:C volume ratio as cells with round nuclei. This indicates that something other than the availability of the NE couples cell size to nuclear size.

The original budding yeast study on N:C volume ratio (Jorgensen *et al.*, 2007) examined cells under different conditions, including mutants with small cell size, but in that study nuclear shape was not assessed. In search of other conditions that restrict cell size, we examined a number of small cell size mutants, including *whi3*Δ, *whi5*Δ, *swe1*Δ, and *sfp1*Δ (Jorgensen *et al.*, 2002). We confirmed that these mutants have the same N:C volume ratio as wild-type cells, as reported by Jorgensen *et al.* (2007) and unpublished data. Of these mutants, only *sfp1*Δ mutant cells had abnormally shaped nuclei, as quantified by sphericity (Figure 10, A and B). Why don't all small cells have deformed nuclei? The explanation may lie in the relationship between NE expansion and growth rate rather than cell size per se. The absence of Whi3 and Whi5 causes a premature passage through START, while the absence of Swe1 causes a premature entry into mitosis, but the actual growth rate of these mutants is normal (Sia *et al.*, 1996; Nash *et al.*, 2001; Harvey and Kellogg, 2003; Costanzo *et al.*, 2004). Thus, in these strains the rate of NE expansion might not exceed the rate of cell growth. In contrast, *sfp1*Δ cells exhibit a slow growth rate (Blumberg and Silver, 1991), which could cause a build-up of excess NE relative to cells size, leading to nuclear deformation. Sfp1 is a nutrient-sensitive transcription factor that regulates the expression of ribosome biogenesis genes (Jorgensen *et al.*, 2002, 2004), with no known connection to lipid metabolism. Nonetheless, it remains to be determined whether absence of Sfp1 also affects NE expansion independently.

DISCUSSION

The scaling of nuclear and cell volumes is a fascinating yet poorly understood phenomenon. In the present study, we examined whether the NE could be the nuclear factor that regulates nuclear size. By inhibiting cell growth using secretion mutants, we were able to demonstrate that NE expansion is not linked to cell size. When cell growth is inhibited the N:C ratio is kept constant, accommodating the expanding NE by nuclear shape deformation from spherical to bilobed. This conclusion is predicated on the NE expanding normally in the secretion mutants used in this study. Two lines of evidence suggest that this is indeed the case: 1) the structure of the ER in the secretion mutants used here is normal (Novick *et al.*, 1980; Prinz *et al.*, 2000) (Figure 2), suggesting that these mutations do not cause abnormal ER/NE expansion, and 2) bilobed nuclei occur preferentially in cells that have separate SPBs, suggesting that bilobed nuclei are a result of NE expansion that occurs as it normally would during the cell cycle (Figure 5). This is unlike the nuclear deformations due to NE expansion in *spo7*Δ mutants, which are a result of increase phospholipid biosynthesis that leads to altered ER structure and nuclear deformations throughout the cell cycle (Campbell *et al.*, 2006).

The bilobed nuclear phenotype of the *sec* mutants used here adds to a growing list of conditions in budding yeast in which NE expansion is coupled to a deformation in the nucleolar compartment. These include a mitotic delay (Witkin *et al.*, 2012) and down-regulation of the lipin pathway (Campbell *et al.*, 2006), both of which lead to a NE extension, or flare, adjacent to the nucleolus. We have previously shown that while the nucleolus is not needed for the mitotic flare to form, the length or compaction of the ribosomal DNA (rDNA) can affect the shape of the flare (Walters *et al.*, 2014). For example, in condensin mutants, which alter the compaction of the rDNA, the flare is more "stubby" compared with mitotic nuclear flares observed in wild-type cells (Walters *et al.*, 2014). Inhibition of secretion has been shown to down-regulate ribosome synthesis due to activation of the cell wall integrity pathway and repression of the TOR pathway (Mizutat and Warner, 1994; Li *et al.*, 2000; Singh and Tyers, 2009). While not directly tested for the mutants used in the present study, it is possible that at 34°C, these *sec* mutations lead to down-regulation of ribosome synthesis that contributed, at least in part, to the growth defect (Supplemental Figure S1B and unpublished data). Thus, the bilobe could be a manifestation of a nuclear flare but with an altered shape due to reduced ribosome synthesis and hence altered nucleolar morphology. That said, the *sec*-dependent nuclear bilobe is distinct from both the *spo7*Δ flare and the mitotic flare: unlike *spo7*Δ flares, the *sec* mutant–dependent nuclear bilobes are cell-cycle dependent (Figure 5), and the mitotic flare, but not the bilobe, is dependent on Cdc5 activity (Supplemental Figure S4A). The fact that the nuclear deformity in all of the above cases coincides with the location of the nucleolus is, in itself, an extremely interesting phenomenon that warrants further study.

Our study highlights two potential causes for abnormal nuclear morphology. Because the NE can expand independently of cell size, and under conditions where nuclear volume scales with cell volume, irregularly shaped nuclei can happen in one of two ways: first, NE expansion can be accelerated due, for example, to increased phospholipid synthesis, such as in the case of *spo7*Δ cells and

perhaps cycloheximide treatment. Under these conditions the nuclear surface area becomes abnormally large while the increase in nuclear content lags behind, resulting in a deformed nucleus. Alternatively, NE expansion can occur as it normally would by following the appropriate cell-cycle cues, but cell growth can be attenuated, as in the case of *sec* mutants. Thus, in circumstances of altered nuclear morphology, such as in cells of aged individuals, one needs to determine whether the N:C volume is maintained and, if so, whether the underlying defect leading to altered nuclear shape is enhanced NE expansion or reduced cell growth.

Our findings differ from those of Kume *et al.* (2017), who concluded that in fission yeast the NE contributes to nuclear volume. This was based on the finding that misregulated phospholipid synthesis in lipin pathway mutants increased the N:C volume ratio. There are two possible reasons for the difference between the Kume *et al.* study and the present one: first, the regulation of nuclear volume may differ between budding yeast and fission yeast, as three-dimensional reconstructions of the *spo7*Δ nucleus in budding yeast showed that this mutant exhibits the same N:C volume ratio as wild-type cells (Webster *et al.*, 2010). Second, lipin pathway mutants (*spo7*Δ, *nem1*Δ, and *pah1*Δ/*ned1*Δ in budding and fission yeast, respectively) exhibit an abnormally shaped nucleus in both yeasts (Tange *et al.*, 2002; Santos-Rosa *et al.*, 2005). Kume *et al.* (2017) calculated nuclear volumes by measuring nuclear axes and assuming the nucleus is a prolate sphere, following the methodology described by Neumann *et al.* (2007). It is possible that the abnormal shape of the nucleus led the authors to overestimate nuclear volume, resulting in an apparent increase in the N:C volume ratio.

Taken together, our study suggests that NE expansion is not linked to cell size and does not determine nuclear size. This leaves the nucleoplasm as a determinant of nuclear volume. How might one or more components of the nucleoplasm be linked to cell size? An attractive possibility is that the synthesis of nuclear proteins (and perhaps that of cellular proteins in general) somehow scale with cell size and that the bulk nuclear protein mass determines the volume of the nucleus. In other words, NE expansion may proceed according to cell-cycle cues, but the amount of nuclear proteins that fill the NE is dictated by cell size. Since cell size often tracks with cell-cycle progression, this will usually result in a spherical, or nearly spherical, nucleus. This model is consistent with one of Kume *et al.*'s observations that inhibition of mRNA export leads to a higher N:C volume ratio coincidently with higher representation of nuclear proteins in the nucleoplasm (Kume *et al.*, 2017). This model is also consistent with the requirement for nuclear import in maintaining a normal N:C volume ratio component, lamin A, that was suggested to be a key scaling factor in *Xenopus* egg extracts. While our data rule out the availability of the NE as a limiting factor in determining nuclear volume, it is still possible that one or more factors associated with the NE could affect the size of the nucleus. For example, nuclear import or export could play a role in controlling the amount of protein in the nucleus, thereby affecting nuclear size. How NE expansion is regulated in budding yeast remains an interesting question, but our study shows that it is not a simple consequence of cell size. Moreover, our study has limited the possible options for factors that regulate nuclear volume, at least in budding yeast, to the nucleoplasm, and it now remains to be determined whether a specific protein(s) or bulk nuclear protein regulate nuclear size.

MATERIALS AND METHODS

Media and growth conditions

Strains containing plasmids were initially grown in synthetic complete (SC) media lacking the appropriate amino acid to allow plasmid selection (Webster *et al.*, 2010). For temperature shift experiments, cells were grown at 23°C to early log phase and then switched from SC media into yeast extract/peptone/dextrose (YPD) media (Webster *et al.*, 2010) for 2 h at 23°C before being incubated at 23°, 34°, or 37°C for the indicated periods of time. To inhibit fatty acid synthesis, cerulenin (Sigma) was added a final concentration of 2 µg/ml, and cells were incubated at 23°C or 34°C for 2 h. Cycloheximide (Sigma) was used at 0.33 mg/ml. For cells grown in YPD, cycloheximde was added from a 100 mg/ml stock in ethanol. For cells grown in SC media, cycloheximide was dissolved directly in the media in its final concentration (0.33 mg/ml). Rapamycin (Sigma) was used at 10 µM. For galactose induction of *SPO7* and *NEM1*, cells were grown overnight in SC media lacking adenine, leucine, and uracil and containing raffinose as a carbon source. Cell were switched to YP media + raffinose for 1 h and then treated with galactose for 1 h before shifting them to 34°C for 2 h. G1 arrest was induced using 20 µM alpha-factor (Zymo Research).

Strains and plasmids

The strains used in this study are listed in Supplemental Table S4. Strains were constructed via crosses or by homology-directed integration (Longtine *et al.*, 1998). Strains carrying *RTN1-GFP* were constructed by homology directed integration, using the endogenously GFP-tagged *RTN1* gene in the yeast GFP collection (Thermo Fisher) as PCR template with the following primers: 5′-GTTCTCTATCTGGACCATC and 5′-CAACTAGAGGTTTCTAGTGG. Strains carrying DsRED-HDEL were constructed by integrating the pWP1435 plasmid (YIPlac *DsRED-HDEL::NAT TRP1*; a generous gift from Will Prinz [National Institutes of Health/National Institute of Diabetes and Digestive and Kidney Diseases], derived from pKW1803 [Madrid *et al.*, 2006]) at the *TRP1* locus by cutting the plasmid with *Eco*RV. *sec6-4*, *sec9-4*, and *sec15-1* mutations were confirmed by sequencing after they were moved from the temperature sensitive mutant collection background (Li *et al.*, 2011) (S288C) into the W303 background via homology directed integration. Plasmid pPUS1-GFP-URA is a CEN-based plasmid described in (Webster *et al.*, 2010) and was used for visualization of the nucleoplasm. Strains AWY186 and AWY187 were generated by transformation of WT and *sec6-4* strains with plasmid pASZ11-NupNop, a CEN *ADE2*-based plasmid expressing *GFP-NUP49* and *mCherry-NOP1* (Berger *et al.*, 2008), followed by deletion of the endogenous *NUP49* gene via homology directed integration of *NATMX* (Goldstein and McCusker, 1999) at the *NUP49* locus. Plasmids expressing *GAL-SPO7* and *GAL-NEM1* were described in Siniossoglou *et al.* (1998) and Witkin *et al.* (2012).

Fluorescence microscopy and measurements

Quantification of ER expansion was done as described by Shibata *et al.* (2010). Briefly, cells were grown in SC media to OD 0.2 and then shifted to 34°C for 2 h. Cells (1.5 µl) were mounted directly on a glass slide and covered by a coverslip. Images of live cells were taken on a Nikon E800 microscope equipped with a Yokogawa CSU10 spinning disk, a Hamamatsu Orca-flash4.0LT camera, and MetaMorph 7.8.8.0 (Molecular Devices, Sunnyvale, CA) software, using a plan Apo 100×/1.4 NA objective. Images were analyzed using the MetaMorph colocalization function as described by Shibata *et al.* (2010). Merge images were generated using ImageJ (National Institutes of Health).

To score nuclear phenotypes, cells were fixed by incubation in 4% paraformaldehyde for 1 h at 23°C on a roller drum and then washed several times in 1x phosphate-buffered saline (PBS). Images of fixed cells were captured by one of two methods: 1) using a microscope (E800; Nikon) equipped with a CFI Apo TIRF 100× oil

objective lens (Nikon) using a charge-coupled device camera (C4742-95; Hamamatsu) operated by iVision software (Biovision Technologies) or 2) using confocal imaging, where fixed cells were incubated with concanavalin A (ConA)-Alexa 655-nm conjugate (ThermoFisher) at room temperature for 1 h, washed with 1x PBS and mixed with an equal volume of vectashield mounting medium and mounted on 3% agarose pads. Images were taken by spinning-disk confocal microscopy using a microscope (Eclipse TE2000U; Nikon) equipped with a CFI Apo TIRF 100× oil objective lens (Nikon) and operated by MetaMorph software (Molecular Devices) using 0.2-µm z intervals. The imaging system also included a spinning-disk unit (CSU10; Yokogawa) and an electron-multiplying–charge coupled device (EM-CCD) camera (C9100-13; Hamamatsu). Prior to the use of sphericty values, a bilobed nucleus was defined as a nucleus with a narrowing (a "waist") or an indentation around the circumference of the nucleus, clearly distinguishable from a normal, spherical nucleus without obvious indentations. In strains where the nucleolus was labeled, bilobed nuclei had a significantly narrower area of contact between the nucleolus and the rest of the nucleus compared with round nuclei.

For time-lapse fluorescence microscopy, cells in early log-phase were mounted on 2% or 3% agarose in YPD pads and imaged using the DeltaVision microscope system (GE). Cells were imaged at 34° or 37°C in an environmental chamber including an Olympus IX70 widefield inverted epifluoresence microscope, an Olympus UPlanSapo 100 × NA 1.4 oil immersion objective and a photometrics CCD CoolSnap HQ camera. Images were taken over 20 focal planes using a 0.4-µm step size. A brightfield image was taken at the central focal plane at each time point. Images were deconvolved and maximum intensity projections were generated using SoftWorx (GE). Image processing and analysis were carried out using Imaris (Bitplane). Cell volumes were calculated by measuring cell length and width based on the brightfield image and applying the formula for the volume of a spheroid ($V = 4/3 \times \pi a^2 c$). For budded cells, volumes for mothers and buds were calculated separately then added together to give the total cell volume.

To calculate N:C volume ratios for WT and *sec6-4* from fluorescence images of Nup49-GFP (NucQuant analysis), cells were grown to early log-phase in YPD media and then shifted to 34°C for 1 h. Cells were washed once in SC media, mounted on an agarose SC pad, and imaged live within 20 min on a spinning disk confocal microscope as described in Wang *et al.* (2016). NPC maps and reconstructions of nuclei from WT and *sec6-4* cells were generated from confocal images as described in Wang *et al.* (2016). For *sec6-4*, only cells displaying the bilobed nuclear phenotype were included in the analysis. Cell size was measured using the cytoplasmic pool of mCherry-Nop1, and cell volume was calculated as above.

To calculate N:C volume ratio and sphericity for WT, *sec6-4*, and *sec15-1* cells using Pus1-GFP, cells were grown overnight at 23°C to early log phase in SC media without uracil, switched to YPD for 2 h, and then shifted to 34°C for 1 h. Cells were fixed, stained for ConA conjugated to AlexaFluor-655 and imaged by confocal microscopy as described in Webster *et al.* (2010). Cell size was measured using the ConA signal and calculated as described above. Nuclear size and sphericity were determined using Imaris software (Bitplane, Concord, MA) as described in Webster *et al.* (2010).

Soft X-ray microscopy

Soft X-ray imaging and image processing were carried out as in Uchida *et al.* (2011) and Parkinson *et al.* (2012). X-ray data sets were collected using the XM-2 soft X-ray microscope operated by the National Center for X-ray Tomography (http://ncxt.lbl.gov) at the Advanced Light Source (www.als.lbl.gov) of Lawrence Berkeley National Laboratory (LBNL). The XM-2 soft X-ray microscope is equipped with Fresnel zone plate-based condenser and objective lenses (made by the Center for X-ray Optics, LBNL). The objective lens is the resolution-defining element of this microscope; these data used a zone plate with a 50-nm outer zone width. To prepare specimens for soft X-ray tomography, cells were rapidly transferred from their growth media to thin-walled glass capillaries and immediately vitrified by plunge-freezing in ~90 K liquid propane. Soft X-ray tomography imaging was performed with the specimens in an atmosphere of helium gas cooled by liquid nitrogen. For each data set, 90 projection images were collected sequentially around a rotation axis in 2° increments, giving a total rotation of 180°. Exposure time varied between 150 and 300 ms, depending on the capillary thickness. Projection images were aligned, and tomographic reconstructions calculated using the AREC-3D package (Parkinson *et al.*, 2012). Manual segmentation of cells and visualizations of nuclear and cell surface areas were carried out using Amira software (FEI Visualization Sciences Group). Nuclear sphericity was calculated using the formula $\Psi = \pi^{1/3}(6V_p)^{2/3}/A_p$, where V_p = nuclear volume and A_p = nuclear surface area.

Statistical analyses

Statistical analyses were performed using Prism software (Graphpad software, La Jolla CA). The number of cells scored, biological replicates, and the types of tests performed are indicated in the figure legends.

ACKNOWLEDGMENTS

We thank Julie Cooper and Manasi Apte for assistance using the DeltaVision; Jonathan Fix for assistance with statistical analyses; Mary Munson, Will Prinz, and Brenda Andrews for strains; and Will Prinz, Mark Rose, Michael Lichten, and members of the Cohen-Fix lab for fruitful discussions. This work was funded by intramural National Institute of Diabetes and Digestive and Kidney Diseases grant #DK057807 to O.C.F. O.G. was supported by an Agence Nationale de la Recherche grant (ANDY) and Initiative d'excellence of Université de Toulouse (Clemgene and Nudgene). The National Center for X-ray Tomography (C.A.L., J.C., and G.M.) is supported by the National Institutes of Health (P41GM103445), DOE's Office of Biological and Environmental Research (DE-AC02-5CH11231), and the Gordon and Betty Moore Foundation (3497).

REFERENCES

Anastasia SD, Nguyen DL, Thai V, Meloy M, MacDonough T, Kellogg DR (2012). A link between mitotic entry and membrane growth suggests a novel model for cell size control. J Cell Biol 197, 89–104.

Bell ES, Lammerding J (2016). Causes and consequences of nuclear envelope alterations in tumour progression. Eur J Cell Biol 95, 449–464.

Berger AB, Cabal GG, Fabre E, Duong T, Buc H, Nehrbass U, Olivo-Marin J-C, Gadal O, Zimmer C (2008). High-resolution statistical mapping reveals gene territories in live yeast. Nat Methods 5, 1031–1037.

Blank HM, Perez R, He C, Maitra N, Metz R, Hill J, Lin Y, Johnson CD, Bankaitis VA, Kennedy BK, *et al.* (2017). Translational control of lipogenic enzymes in the cell cycle of synchronous, growing yeast cells. EMBO J 36, 487–502.

Blumberg H, Silver PA (1991). A split zinc-finger protein is required for normal yeast growth. Gene 107, 101–110.

Bombardier JP, Munson M (2015). Three steps forward, two steps back: mechanistic insights into the assembly and disassembly of the SNARE complex. Curr Opin Chem Biol 29, 66–71.

Bucci M, Wente SR (1997). In vivodynamics of nuclear pore complexes in yeast. J Cell Biol 136, 1185–1199.

Campbell JL, Lorenz A, Witkin KL, Hays T, Loidl J, Cohen-Fix O (2006). Yeast nuclear envelope subdomains with distinct abilities to resist membrane expansion. Mol Biol Cell 17, 1768–1778.

Carman GM, Han GS (2018). Phosphatidate phosphatase regulates membrane phospholipid synthesis via phosphatidylserine synthase. Adv Biol Regul 67, 49–58.
Cavanaugh AM, Jaspersen SL (2017). Big lessons from little yeast: budding and fission yeast centrosome structure, duplication, and function. Annu Rev Genet 51, 361–383.
Chan Y-HM, Marshall WF (2010). Scaling properties of cell and organelle size. Organogenesis 6, 88–96.
Chow K-H, Factor RE, Ullman KS (2012). The nuclear envelope environment and its cancer connections. Nat Rev Cancer 12, 196–209.
Costanzo M, Nishikawa JL, Tang X, Millman JS, Schub O, Breitkreuz K, Dewar D, Rupes I, Andrews B, Tyers M (2004). CDK activity antagonizes Whi5, an inhibitor of G1/S transcription in yeast. Cell 117, 899–913.
Dubots E, Cottier S, Péli-Gulli M-P, Jaquenoud M, Bontron S, Schneiter R, De Virgilio C (2014). TORC1 regulates Pah1 phosphatidate phosphatase activity via the Nem1/Spo7 protein phosphatase complex. PLoS One 9, e104194.
Duden R, Hosobuchi M, Hamamoto S, Winey M, Byers B, Schekman R (1994). Yeast β-and β′-Coat Proteins (COP). Two coatomer subunits essential for endoplasmic reticulum-to-Golgi protein traffic. J Biol Chem 269, 24486–24495.
Feyder S, De Craene J-O, Bär S, Bertazzi D, Friant S (2015). Membrane trafficking in the yeast *Saccharomyces cerevisiae* model. Int J Mol Sci 16, 1509–1525.
Golden A, Liu J, Cohen-Fix O (2009). Inactivation of the *C. elegans* lipin homolog leads to ER disorganization and to defects in the breakdown and reassembly of the nuclear envelope. J Cell Sci 122, 1970–1978.
Goldstein AL, McCusker JH (1999). Three new dominant drug resistance cassettes for gene disruption in *Saccharomyces cerevisiae*. Yeast 15, 1541–1553.
Gonzalez Y, Meerbrey K, Chong J, Torii Y, Padte NN, Sazer S (2009). Nuclear shape, growth and integrity in the closed mitosis of fission yeast depend on the Ran-GTPase system, the spindle pole body and the endoplasmic reticulum. J Cell Sci 122, 2464–2472.
Gorjánácz M, Mattaj IW (2009). Lipin is required for efficient breakdown of the nuclear envelope in *Caenorhabditis elegans*. J Cell Sci 122, 1963–1969.
Han G-S, Carman GM (2017). Yeast PAH1-encoded phosphatidate phosphatase controls the expression of CHO1-encoded phosphatidylserine synthase for membrane phospholipid synthesis. J Biol Chem 292, 13230–13242.
Han G-S, Wu W-I, Carman GM (2006). The *Saccharomyces cerevisiae* Lipin homolog is a Mg2+-dependent phosphatidate phosphatase enzyme. J Biol Chem 281, 9210–9218.
Hara Y, Merten CA (2015). Dynein-based accumulation of membranes regulates nuclear expansion in *Xenopus laevis* egg extracts. Dev Cell 33, 562–575.
Harvey SL, Kellogg DR (2003). Conservation of mechanisms controlling entry into mitosis: budding yeast Wee1 delays entry into mitosis and is required for cell size control. Curr Biol 13, 264–275.
Heider MR, Munson M (2012). Exorcising the exocyst complex. Traffic 13, 898–907.
Hereford LM, Hartwell LH (1974). Sequential gene function in the initiation of *Saccharomyces cerevisiae* DNA synthesis. J Mol Biol 84, 445–461.
Higashio H, Kimata Y, Kiriyama T, Hirata A, Kohno K (2000). Sfb2p, a yeast protein related to Sec24p, can function as a constituent of COPII coats required for vesicle budding from the endoplasmic reticulum. J Biol Chem 275, 17900–17908.
Inokoshi J, Tomoda H, Hashimoto H, Watanabe A, Takeshima H, Omura S (1994). Cerulenin-resistant mutants of *Saccharomyces cerevisiae* with an altered fatty acid synthase gene. Mol Gen Genet 244, 90–96.
Jevtic P, Edens LJ, Li X, Nguyen T, Chen P, Levy DL (2015). Concentration-dependent effects of nuclear lamins on nuclear size in Xenopus and Mammalian cells. J Biol Chem 290, 27557–27571.
Jevtic P, Levy DL (2015). Nuclear size scaling during *Xenopus* early development contributes to midblastula transition timing. Curr Biol 25, 45–52.
Johnston GC, Pringle JR, Hartwell LH (1977). Coordination of growth with cell division in the yeast *Saccharomycescerevisiae*. Exp Cell Res 105, 79–98.
Jorgensen P, Edgington NP, Schneider BL, Rupes I, Tyers M, Futcher B (2007). The size of the nucleus increases as yeast cells grow. Mol Biol Cell 18, 3523–3532.
Jorgensen P, Nishikawa JL, Breitkreutz B-J, Tyers M (2002). Systematic identification of pathways that couple cell growth and division in yeast. Science 297, 395–400.
Jorgensen P, Rupes I, Sharom JR, Schneper L, Broach J, Tyers M (2004). A dynamic transcriptional network communicates growth potential to ribosome synthesis and critical cell size. Genes Dev 18, 2491–2505.
Kimata Y, Lim CR, Kiriyama T, Nara A, Hirata A, Kohno K (1999). Mutation of the yeast e-COP gene *ANU2* causes abnormal nuclear morphology and defects in intracellular vesicular transport. Cell Struc Func 24, 197–208.
Kume K, Cantwell H, Neumann FR, Jones AW, Snijders AP, Nurse P (2017). A systematic genomic screen implicates nucleocytoplasmic transport and membrane growth in nuclear size control. PLoS Genet 13, e1006767.
Ladouceur A-M, Dorn JF, Maddox PS (2015). Mitotic chromosome length scales in response to both cell and nuclear size. J Cell Biol 209, 645–652.
Le Gros MA, McDermott G, Larabell CA (2005). X-ray tomography of whole cells. Curr Opin Struct Biol 15, 593–600.
Lempiainen H, Uotila A, Urban J, Dohnal I, Ammerer G, Loewith R, Shore D (2009). Sfp1 interaction with TORC1 and Mrs6 reveals feedback regulation on TOR signaling. Mol Cell 33, 704–716.
Levy DL, Heald R (2010). Nuclear size is regulated by Importin α and Ntf2 in *Xenopus*. Cell 143, 288–298.
Li UN, Moir RD, Sethy-Coraci IK, Warner JR, Willis IM (2000). Repression of ribosome and tRNA synthesis in secretion-defective cells is signaled by a novel branch of the cell integrity pathway. Mol Cell Biol 20, 3843–3851.
Li Z, Vizeacoumar FJ, Bahr S, Li J, Warringer J, Vizeacoumar FS, Min R, Vandersluis B, Bellay J, Devit M, *et al*. (2011). Systematic exploration of essential yeast gene function with temperature-sensitive mutants. Nat Biotechnol 29, 361–367.
Longtine MS, McKenzie A III, Demarini DJ, Shah NG, Wach A, Brachat A, Philippsen P, Pringle JR (1998). Additional modules for versatile and economical PCR-based gene deletion and modification in *Saccharomyces cerevisiae*. Yeast 14, 953–961.
Madrid AS, Mancuso J, Cande WZ, Weis K (2006). The role of the integral membrane nucleoporins Ndc1p and Pom152p in nuclear pore complex assembly and function. J Cell Biol 173, 361–371.
Matynia A, Salus SS, Sazer S (2002). Three proteins required for early steps in the protein secretory pathway also affect nuclear envelope structure and cell cycle progression in fission yeast. J Cell Sci 115, 421–431.
McDermott G, Le Gros MA, Larabell CA (2012). Visualizing cell architecture and molecular location using soft X-ray tomography and correlated cryo-light microscopy. Annu Rev Phys Chem 63, 225–239.
Mizutat K, Warner JR (1994). Continued functioning of the secretory pathway is essential for ribosome synthesis. Mol Cell Biol 14, 2493–2502.
Mukherjee RN, Chen P, Levy DL (2016). Recent advances in understanding nuclear size and shape. Nucleus 7, 167–186.
Nanduri J, Mitra S, Andrei C, Liu Y, Yu Y, Hitomi M, Tartakoff AM (1999). An unexpected link between the secretory path and the organization of the nucleus. J Biol Chem 274, 33785–33789.
Nash RS, Volpe T, Futcher B (2001). Isolation and characterization of WHI3, a size-control gene of *Saccharomyces cerevisiae*. Genetics 157, 1469–1480.
Neumann FR, Nurse P (2007). Nuclear size control in fission yeast. J Cell Biol 179, 593–600.
Novick P, Field C, Schekman R (1980). Identification of 23 complementation groups required for post-translational yeast secretory pathway. Cell 21, 205–215.
Novick P, Schekman R (1979). Secretion and cell-surface growth are blocked in a temperature-sensitive mutant of *Saccharomyces cerevisiae*. Proc Natl Adac Sci 76, 1858–1862.
O'Hara L, Han G-S, Peak-Chew S, Grimsey N, Carman GM, Siniossoglou S (2006). Control of phospholipid synthesis by phosphorylation of the yeast Lipin Pah1p/Smp2p. J Biol Chem 281, 34537–34548.
Parkinson DY, Knoechel C, Yang C, Larabell CA, Le Gros MA (2012). Automatic alignment and reconstruction of images for soft X-ray tomography. J Struc Biol 177, 259–266.
Perry RJ, Mast FD, Rachubinski RA (2009). Endoplasmic reticulum-associated secretory proteins Sec20p, Sec39p, and Dsl1p are involved in peroxisome biogenesis. Euk Cell 8, 830–843.
Prinz WA, Grzyb L, Veenhuis M, Kahana JA, Silver PA, Rapoport TA (2000). Mutants affecting the structure of the cortical endoplasmic reticulum in *Saccharomyces cerevisiae*. J Cell Biol 150, 461–474.
Ramirez RM, Ishida-Schick T, Krilowicz BL, Leish BA, Atkinson KD (1983). Plasma membrane expansion terminates in Saccharomyces cerevisiae

secretion-defective mutants while phospholipid synthesis continues. J Bacteriol 154, 1276–1283.
Ryan KJ, Wente SR (2002). Isolation and characterization of new *Saccharomyces cerevisiae* mutants perturbed in nuclear pore complex assembly. BMC Genetics 3, 17.
Santos-Rosa H, Leung J, Grimsey N, Peak-Chew S, Siniossoglou S (2005). The yeast lipin Smp2 couples phospholipid biosynthesis to nuclear membrane growth. EMBO J 24, 1931–1941.
Schuck S, Prinz WA, Thorn KS, Voss C, Walter P (2009). Membrane expansion alleviates endoplasmic reticulum stress independently of the unfolded protein response. J Cell Biol 187, 525–536.
Shibata Y, Shemesh T, Prinz WA, Palazzo AF, Kozlov MM, Rapoport TA (2010). Mechanisms determining the morphology of the peripheral ER. Cell 143, 774–788.
Sia RAL, Herald HA, Lew DJ (1996). Cdc28 tyrosine phosphorylation and the morphogenesis checkpoint in budding yeast. Mol Biol Cell 7, 1657–1666.
Singh J, Tyers M (2009). A Rab escort protein integrates the secretion system with TOR signaling and ribosome biogenesis. Genes Dev 23, 1944–1958.
Siniossoglou S, Santos-Rosa H, Rappsilber J, Mann M, Hurt E (1998). A novel complex of membrane proteins required for formation of a spherical nucleus. EMBO J 17, 6449–6464.
Tange Y, Hirata A, Niwa O (2002). An evolutionarily conserved fission yeast protein, Ned1, implicated in normal nuclear morphology and chromosome stability, interacts with Dis3, Pim1/RCC1 and an essential nucleoporin. J Cell Sci 115, 4375–4385.
Uchida M, Sun Y, McDermott G, Knoechel C, Le Gros MA, Parkinson D, Drubin DG, Larabell CA (2011). Quantitative analysis of yeast internal architecture using soft Xray tomography. Yeast 28, 227–236.
Urban J, Soulard A, Huber A, Lippman S, Mukhopadhyay D, Deloche O, Wanke V, Anrather D, Ammerer G, Riezman H, *et al*. (2007). Sch9 is a major target of TORC1 in *Saccharomyces cerevisiae*. Mol Cell 26, 663–674.
Vadia S, Tse JL, Lucena R, Yang Z, Kellogg DR, Wang JD, Levin PA (2017). Fatty acid availability sets cell envelope capacity and dictates microbial cell size. Curr Biol 27, 1757–1767.
Vukovic LD, Jevtic P, Zhang Z, Stohr BA, Levy DL (2016). Nuclear size is sensitive to NTF2 protein levels in a manner dependent on Ran binding. J Cell Sci 129, 1115–1127.
Wadell H (1935). Volume, shape and roundness of quartz particles. J Geol 43, 250–280.
Walters AD, Bommakanti A, Cohen-Fix O (2012). Shaping the nucleus: Factors and forces. J Cell Biochem 113, 2813–2821.
Walters AD, May CK, Dauster ES, Cinquin BP, Smith EA, Robellet X, D'Amours D, Larabell CA, Cohen-Fix O (2014). The yeast polo kinase Cdc5 regulates the shape of the mitotic nucleus. Curr Biol 24, 2861–2867.
Wang R, Kamgoue A, Normand C, Léger-Silvestre I, Mangeat T, Gadal O (2016). High resolution microscopy reveals the nuclear shape of budding yeast during cell cycle and in various biological states. J Cell Sci 129, 4480–4495.
Webster MT, McCaffery JM, Cohen-Fix O (2010). Vesicle trafficking maintains nuclear shape in *Saccharomyces cerevisiae* during membrane proliferation. J Cell Biol 191, 1079–1088.
Winey M, Yarar D, Giddings TH, Mastronarde DN (1997). Nuclear pore complex number and distribution throughout the *Saccharomyces cerevisiae* cell cycle by three-dimensional reconstruction from electron micrographs of nuclear envelopes. Mol Biol Cell 8, 2119–2132.
Witkin KL, Chong Y, Shao S, Webster MT, Lahiri S, Walters AD, Lee B, Koh JL, Prinz WA, Andrews BJ, Cohen-Fix O (2012). The budding yeast nuclear envelope adjacent to the nucleolus serves as a membrane sink during mitotic delay. Curr Biol 22, 1128–1133.
Yam C, He Y, Zhang D, Chiam K-H, Oliferenko S (2011). Divergent strategies for controlling the nuclear membrane satisfy geometric constraints during nuclear division. Curr Biol 21, 1314–1319.